Ghost optical coherence tomography

CAROLINE G. AMIOT,[1,2,*] **PIOTR RYCZKOWSKI,**[1] **ARI T. FRIBERG,**[3] **JOHN M. DUDLEY,**[2] **AND GOËRY GENTY**[1]

[1]*Laboratory of Photonics, Physics Unit, Tampere University, 33720 Tampere, Finland*
[2]*Institut FEMTO-ST, UMR 6174 CNRS, Université de Bourgogne Franche-Comté, 15 avenue des Montboucons, 25000 Besançon, France*
[3]*Department of Physics and Mathematics, University of Eastern Finland, 80100 Joensuu, Joensuu, Finland*
[*]*caroline.amiot@tuni.fi*

Abstract: We demonstrate experimentally ghost optical coherence tomography using a broadband incoherent supercontinuum light source with shot-to-shot random spectral fluctuations. The technique is based on ghost imaging in the spectral domain where the object is the spectral interference pattern generated from an optical coherence tomography interferometer in which a physical sample is placed. The axial profile of the sample is obtained from the Fourier transform of the correlation between the spectrally resolved intensity fluctuations of the supercontinuum and the integrated signal measured at the output of the interferometer. The results are in excellent agreement with measurements obtained from a conventional optical coherence tomography system.

1. Introduction

Optical coherence tomography (OCT) is an interferometric imaging technique commonly used to obtain images with high in-depth resolution [1–3]. Due to its non-invasive character and the absence of ionizing radiation or toxic contrast agents in its implementation, OCT has found immediate biomedical applications and it is now widely used in retinal, skin, and blood vessel examination [4–7]. OCT is also sometimes used in industrial applications for the characterization of materials and components [8]. A particular variant of OCT performed in the spectral (wavelength) domain is based on measuring the phase relation between different wavelength components of a broadband light source in order to determine the distance to the sample under test [9]. A major benefit of spectral-domain OCT is that it does not require scanning along the sample direction, allowing for significantly faster acquisition speeds compared to its time-domain counterpart [10]. Spectral-domain OCT has been demonstrated using various types of light sources including broadband stationary sources, pulsed lasers, or swept-wavelength sources [11].

In parallel to the rapid development in OCT technologies, there has also been recently interest in the unconventional imaging technique known as ghost imaging [12, 13]. Ghost imaging is based on the principle of image creation from the correlation between a known structured pattern that illuminates an object and the total integrated intensity transmitted (or reflected) by the object. Ghost imaging can be performed using light sources with random intensity patterns [14], in which case patterns need to be measured, or patterns which are pre-programmed and projected using e.g. digital micro-mirrors [15–18].

The defining feature of ghost imaging is that neither the illuminating patterns nor the integrated intensity alone actually carry enough information to reconstruct the image. Rather, it is only by correlating the two measurements of the structured illuminating source and the integrated intensity from the object that an image can be generated. In this regard, the fact that the light actually detected from the object is integrated intensity has also led to ghost imaging being referred to as single-pixel imaging. A significant advantage of ghost imaging when compared to conventional imaging is that it is insensitive to distortions of the wavefront occurring after

the object as only the total light intensity is measured [19], making it ideal for measurements in turbid media or in the presence of other noise [20]. Ghost imaging has also been extended to the temporal domain [20–22] and very recently in the wavelength domain for broadband greenhouse-gas spectroscopic measurements [23].

In this work, we extend the concept of spectral-domain ghost imaging demonstrated in [23] to Fourier-domain OCT and introduce the concept of ghost optical coherence tomography. This approach generates a "ghost" spectral interferogram from the correlation between the spectrally-resolved intensity fluctuations of a noisy supercontinuum source and the integrated signal measured at the output of an OCT interferometer where a physical sample is placed. As in conventional OCT, the axial profile of the sample is then retrieved from the Fourier transform of the interferogram. Because the spectral ghost imaging approach produces the very same interferogram as in conventional OCT, the signal scattered from the sample is similarly "coherently amplified" by the reference arm.

As a proof-of-principle demonstration, we characterize the relative displacement of a perfectly reflecting mirror and perform measurement of the thickness of a microscope cover glass. The results are in excellent agreement with those obtained from a conventional OCT setup. Compared to a conventional OCT apparatus, a significant advantage of the ghost OCT scheme is that it does not require any particularly sensitive detector or spectrometer at the interferometer output. While the performances of the system in terms of axial resolution, imaging depth, and speed can be certainly improved by using tailored supercontinuum sources, the concept can be very useful in situations where the object is highly absorbing or diffusing, for samples with a low damage threshold or in spectral regions where sensitive detectors or swept sources are not available.

2. Experiments

We begin by illustrating the concept of ghost spectral-domain OCT. To this end, Fig. 1 compares the schematics of a conventional spectral-domain OCT system [Fig. 1(a)] and that of the ghost spectral-domain OCT approach [Fig. 1(b)]. In a conventional OCT system, the beam from a broadband light source is equally divided between the two arms of an equal path Michelson interferometer. The image of the object inserted in one arm is generated by measuring with a high-resolution spectrometer the spectral interference pattern resulting from the superposition of the beams reflected from the reference mirror and object.
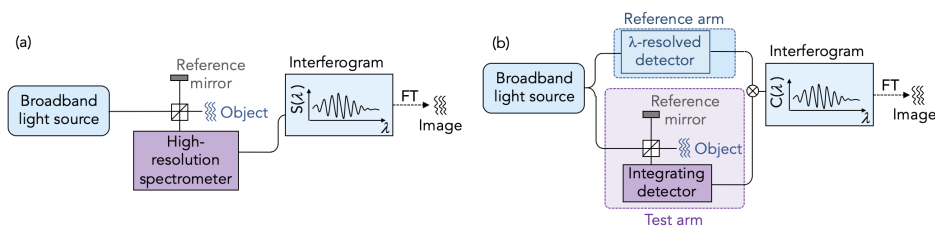

Fig. 1. Schematic illustration of (a) a conventional spectral-domain OCT system and (b) the ghost spectral-domain OCT scheme. FT: Fourier transform.

The axial resolution of the system is inversely proportional the spectral bandwidth $\Delta\lambda$ of the source as $\delta z = 0.44\lambda_0^2/\Delta\lambda$ (for a Gaussian spectral envelope), where λ_0 is the light source center wavelength. The imaging depth is set by the spectrometer resolution. In spectral-domain ghost OCT, the beam from a light source with random spectral intensity fluctuations is divided between a reference arm where the fluctuations are measured in real time and a test arm consisting of an equal-path Michelson interferometer where the object to be measured is placed. The high-resolution spectrometer at the output of the interferometer is replaced by a slow integrating
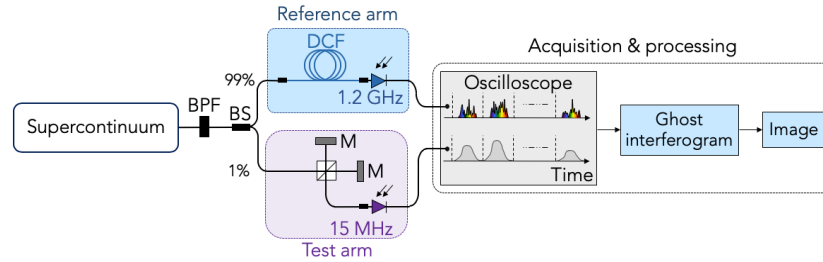
Fig. 2. Experimental setup. BS: beam splitter, BPF: band-pass filter, DCF: dispersion compensating fiber, M: mirror.

detector with no spectral resolution. The "ghost" spectral interference pattern produced by the presence of object in the interferometer is then given by the normalized correlation function $C(\lambda)$ between the reference and test arm signals defined by:

$$C(\lambda) = \frac{\langle \Delta I_{\text{ref}}(\lambda) \times \Delta I_{\text{test}} \rangle_{\text{N}}}{\sqrt{\langle \Delta I_{\text{ref}}^2(\lambda) \rangle_{\text{N}} \langle \Delta I_{\text{test}}^2 \rangle_{\text{N}}}}. \tag{1}$$

Specifically, the normalized wavelength-dependent correlation function $C(\lambda)$ represents correlation between multiple measurements of the spectral intensity fluctuations in the reference arm $I_{\text{ref}}(\lambda)$ and the total (integrated) wavelength-independent intensity I_{test} in the test arm at the output of the interferometer. $\langle \rangle_{\text{N}}$ denotes ensemble average over distinct N realizations, and $\Delta I = I - \langle I \rangle_N$. We emphasize that while the interferogram is retrieved from intensity correlations, the interferogram itself is the manifestation of field correlations just as in conventional OCT. The axial resolution δz of the ghost OCT scheme is identical to that of conventional OCT system and the imaging depth is determined by the resolution with which the spectral intensity fluctuations are measured in the reference arm.

Figure 2 shows our experimental setup. The light source is an incoherent SC extending from ~ 1300 to over 1700 nm and generated by launching 1 kW, 700 ps pulses at 1547 nm with 100 kHz repetition rate (Keopsys-PEFL-K09) into a 6-m long dispersion-shifted fiber (DSF) with zero-dispersion wavelength at 1510 nm (Corning Inc LEAF). The SC generating dynamics arise from noise-seeded modulation instability and soliton dynamics [24], resulting in large and random shot-to-shot spectral fluctuations across the entire SC spectrum [25]. These spectral fluctuations produce the (random) structured patterns that are used to probe the Fourier-domain OCT interferogram. The fact that the supercontinuum source is extremely noisy and unstable is indeed a pre-requisite to the ghost imaging OCT scheme, and the shot-to-shot fluctuations can be conveniently quantified from the coefficient of variation shown in Fig. 3. For convenience, we also plot the SC average spectrum. One can see how the fluctuations are significant and nearly uniform across the entire SC bandwidth with a coefficient of variation close to 50%.

Light from the SC source is divided between the reference and test arms with a 99:1 fiber coupler. The largest fraction is directed through the reference arm due to the large attenuation in the dispersion compensating fiber (DCF, FS.COM customized 150 km) where the spectral fluctuations are measured in real time using the dispersive Fourier transform technique [26,27]. Specifically, the single-shot spectra are converted into the time domain by the 150 km DCF with total dispersion of 3000 ps $\times$ nm^{-1} and measured with 0.2 nm resolution using a 1.2 GHz InGaAs photodetector (Thorlabs DET01CFC/M) and 20 GHz real-time oscilloscope (Tektronix DSA72004) with 6.5 GS/s sampling rate. This corresponds to an imaging depth of 0.3 cm (0.6 cm optical path difference) for which the recovered interferogram fringes visibility drops to 50%.

In order to avoid spectral distortion in the DCF due to attenuation and third-order dispersion,
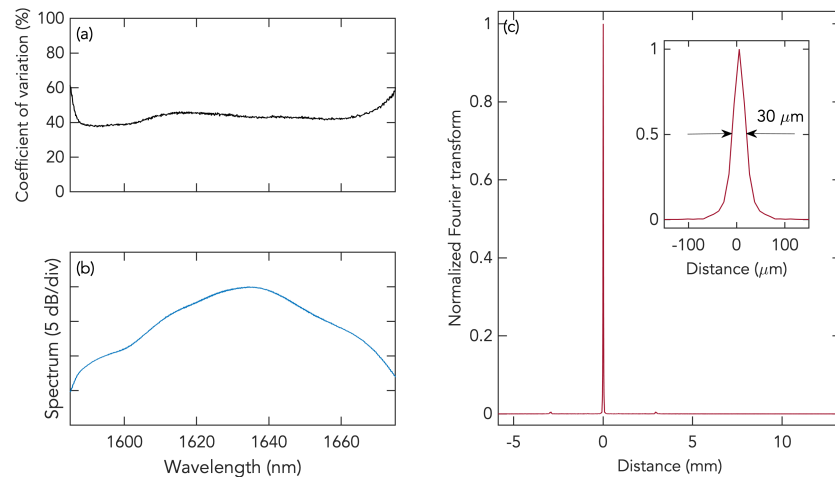
Fig. 3. (a) Coefficient of variation of the supercontinuum fluctuations and (b) supercontinuum average spectrum after the band-pass filter. (c) Average of Fourier transform of the single-shot spectra measured in the reference arm. The inset shows a close-up of the main peak with the FWHM representing the axial resolution limit of the ghost OCT system. The residual peak around 3 mm corresponds to the thickness of the free space filter used before the beam splitter and does not appear in the ghost images as it is not part of the object.

we restrict the SC bandwidth to the 1610-1670 nm range with a bandpass filter (Spectrogon NB-1650-050) corresponding to an axial resolution of ~ 30 µm (see Fig. 3(c)). The output power (average) of the supercontinuum after the spectral filter is 8 mW. In the test arm, light is directed to a standard interferometer whose output intensity is measured with a slow photodetector (15 MHz bandwidth, Thorlabs PDA10D2). The signal from the slow detector is digitized by the oscilloscope at the same sampling rate as that of the reference arm but this is not strictly required, and a lower sampling rate can be used in principle. The single-shot SC spectra from the reference arm and the corresponding spectrally integrated signal from the interferometer are recorded simultaneously by the oscilloscope. The pump laser used for the SC generation has an output port which can be used to trigger the measurement in the reference and test arms. The delay due to different physical lengths of reference and test arms was carefully calibrated using a known modulation pattern and is then compensated in post-processing. The signal from the slow detector is further integrated in post-processing over its full duration span, i.e. over a 30 ns window which allows to reduce the noise and increase the sensitivity in the test arm. The correlation between the single-shot SC spectra and integrated test arm signal computed over multiple realizations then yields the spectral interferogram whose Fourier transform gives the optical path difference between the interferometer arms and thus the axial profile.

3. Results

We first demonstrate the operating principle of ghost OCT by displacing the position of one of the interferometer mirrors from the zero-path difference position. The OCT interferogram is generated from the correlation function between the spectrally-integrated intensity measured at the interferometer output and the intensity of the single-shot SC spectra. The optical path difference (and hence the axial profile) between the two interferometer arms is then simply obtained from the Fourier transform of the interferogram. The results are plotted in Fig. 4 for increasing optical path difference between the mirrors. For comparison, we repeated the same measurements using a conventional OCT scheme by replacing the slow detector at the

output of the OCT interferometer with a high-resolution optical spectral analyzer (OSA, Anritsu MS9740A). The interferogram in this case is measured directly by the OSA and the reference arm measurements are not needed. We can see the excellent correspondence between the ghost and conventional OCT schemes across the full range of measured optical path differences. Due to the difference in the characteristics performance of the slow/fast detectors and OSA, we stress that the conventional OCT results are mostly intended as fidelity measurements rather than as a direct quantitative comparison in terms of performances. The ghost OCT interferogram was generated from 10,000 distinct realizations while the conventional OCT interferogram was measured with the OSA using a virtual bandwidth of 100 Hz corresponding to averaging over 1000 distinct SC realizations. However, the wavelength-by-wavelength measurement of the OSA considerably increases the measurement time of the conventional OCT system which, overall, is 100 times slower than the ghost OCT measurement time. One can also see that the signal-to-noise ratio (SNR) defined as the ratio of the peak to noise floor value is higher by approximately 20 dB in the conventional OCT measurements (Figs. 4 (c) and (d)), however this should be weighted with the sensitivity and dynamic range of the OSA which are significantly better than that of the slow detector used in ghost OCT measurements as well as with the measurement time which is considerably slower.
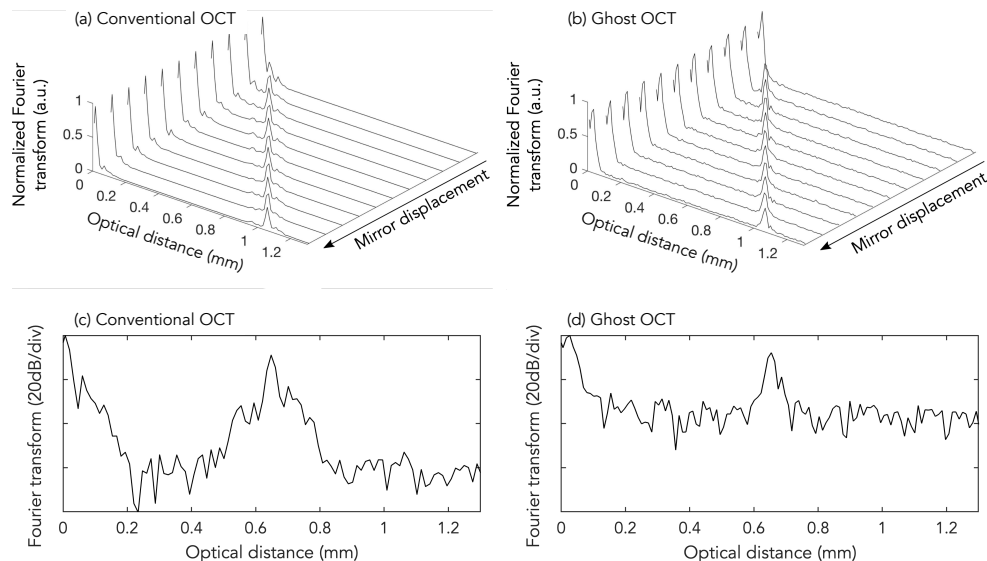

Fig. 4. Optical distance corresponding to half of the optical path difference between the two arms of the Michelson interferometer measured by (a) conventional OCT and (b) the ghost OCT configuration. The arrow indicates the direction of the mirror displacement increasing the optical path difference. The ghost OCT measurements were performed for 10,000 distinct realizations. The conventional OCT measurements performed with the OSA used a virtual bandwidth of 100 Hz corresponding to averaging over 1000 SC pulses. The bottom plots shows the Fourier transform of the interferogram in logarithmic scale for a specific mirror position for (c) conventional OCT and (d) the ghost OCT configuration.

In ghost imaging, the SNR increases with the number of realizations used to compute the correlation, and we illustrate this in Fig. 5 where we show how the Fourier transform of the interferogram evolves as a function of the number of distinct SC pulses for a specific optical path difference (c.a. 0.55 mm in this case) in the interferometer. We can see that even with as few as 200 realizations corresponding to a total recording time of less than 2 ms, and although the SNR is not especially high, the interference fringes are already visible and the optical path difference

can be retrieved. For a larger number of realizations, the SNR increases with the square of the number of realizations [20].
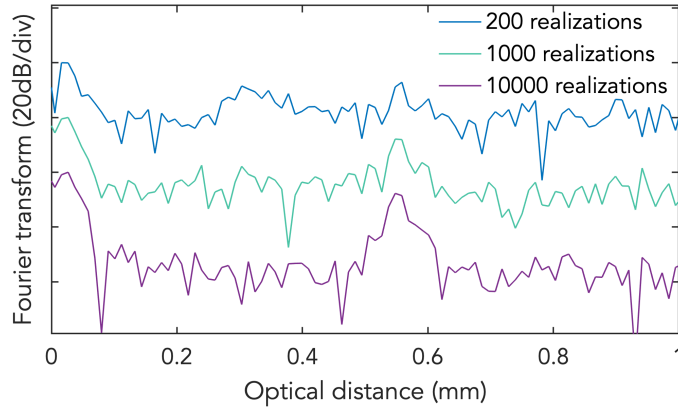

Fig. 5. Fourier transform of the ghost interferogram in logarithmic scale for an optical path difference of 1.1 mm (optical distance of 0.55 mm) between the two arms of the interferometer and for a different number of realizations as indicated. For convenience, the different measurements are arbitrarily shifted vertically.

We next performed a second series of experiments using a dual-interface sample. For this purpose, we replaced one of the mirrors in the interferometer by a 210 µm thick (optical thickness) microscope cover slip consisting of two air-glass interfaces and the optical path difference between the two arms was set to be c.a. 1 mm. The Fourier transform of the resulting interferogram is shown in Fig. 6 both for the conventional OCT system [Fig. 6(a)] and the ghost OCT setup [Fig. 6(b)]. The results are again in excellent agreement and the positions of the two air-glass interfaces can be clearly identified. The distance between the two interfaces is measured to be 220 µm (optical thickness) close to the nominal value of 210 µm provided by the manufacturer.
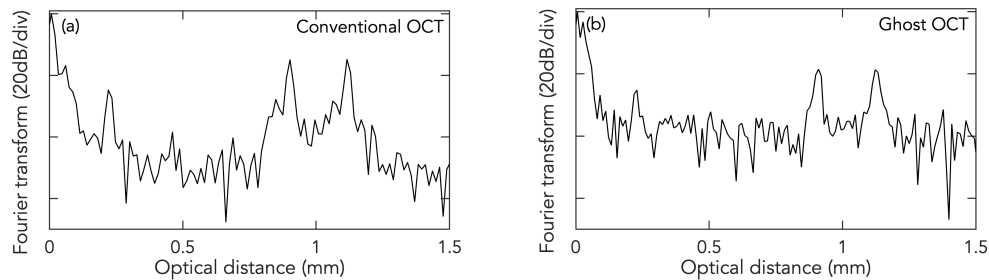

Fig. 6. Fourier transform of the interferogram in logarithmic scale measured by (a) conventional OCT and (b) the ghost OCT configuration when one of the mirrors is replaced by a 210 µm microscope cover slip (optical thickness). The ghost OCT measurements were performed for 10 000 distinct realizations. The conventional OCT measurements performed with the OSA used a virtual bandwidth of 100 Hz corresponding to averaging over 1000 SC pulses.

4. Discussion and conclusions

We have experimentally demonstrated proof-of-concept ghost Fourier-domain OCT in the spectral domain using a broadband, spectrally incoherent, supercontinuum source. As in a conventional

OCT setup, the resolution is determined by the spectral bandwidth of the source. The imaging depth is given by the spectral resolution with which the spectral fluctuations of the light source can be measured in real time (and therefore the total dispersion of the dispersive Fourier transform used for this purpose). The ghost OCT system is robust as the only pre-requisite is that the supercontinuum spectral fluctuations are random, which is the case when using long pump pulses [24].

In principle, one of the benefits of ghost imaging is that it can reduce the number of distinct measurements required as compared to a raster scan, a strategy which is commonly employed e.g. in compressed sensing. In an OCT context, a raster scan is equivalent to the use of a swept-source, requiring high stability and a wavelength-by-wavelength measurement. In addition to the large number of individual wavelength measurements needed, the performances of swept sources-based OCT systems are typically limited by the wavelength coverage and bandwidth tunability of the swept sources, impacting the achievable axial resolution. In contrast, the ghost OCT approach can use any noisy broadband supercontinuum source and thus turn into an advantage a feature which is often detrimental in many applications.

Another advantage of the proposed approach is that it may be particularly efficient in low light level conditions. Indeed, in the ghost imaging scheme, only the total wavelength-integrated signal is measured such that no spectrometer is used after the object to separate the different spectral components as is the case in conventional OCT. This means that in principle the ghost imaging scheme can accommodate a lower intensity signal after the object, such that, if the sample is highly absorbing or diffusing, even a small fraction of the incoming signal may be sufficient to reconstruct the object. Furthermore, unlike in a conventional OCT setup, linear distortions (wavefront, scattering etc...) that may occur at the output of the OCT interferometer (and before the slow detector) do not affect the measured interferogram.

The 'usable' spectral bandwidth of the supercontinuum and therefore the axial resolution of the ghost OCT scheme is limited by the large attenuation at longer wavelengths in the DCF used to measure the spectral fluctuations in real time. Single-shot spectral measurements of octave-spanning supercontinuum have been reported earlier [28] and such large spectral bandwidth would lead to axial resolution at the sub-micron level, significantly better than that can be achieved e.g. with a swept-source. The imaging depth could also be increased by employing a DCF or dispersive element with a larger total dispersion, resulting in improved resolution for the spectral fluctuations measured in real time. Note that using dispersive element with a larger total dispersion would also relax the constraint on the detector speed used in the reference arm.

In the results reported above, the acquisition speed of the ghost OCT setup is limited by the number of realizations (typically 10,000) required to obtain sufficiently high SNR. The overall speed of the system may be increased by using supercontinuum sources with a higher repetition rate. Pump laser with repetition rates up to 100 MHz are commercially available and would lead to a three order of magnitude speed increase, reducing the measurement time to 100 μs per A-scan assuming that about 10,000 distinct realizations are required for high signal-to-noise ratio.

In order to measure 2D or 3D images, the approach requires X-Y scanning as for a conventional OCT setup or swept-source based OCT system. The need for X-Y scan could be eliminated and B or C-scans may be acquired by replacing the slow detector with a line or CCD array and evaluating the correlation between each detector of the array and the fluctuations measured in the reference arm, enabling potentially B or C-scans at tens of kHz speed. One could also possibly exploit the wavelength-dependence of random scattering to eliminate the need for scanning [29].

Finally, we note that the method can be implemented both with classical light sources and entangled photon sources and that a computational version may be realized by using e.g. controllable frequency combs which would completely eliminate the need for single-shot spectral measurements to perform the correlation.

References

1. A. F. Fercher, W. Drexler, C. K. Hitzenberger, and T. Lasser, "Optical coherence tomography-principles and applications," Rep. Prog. Phys. **66**, 239–303 (2003).
2. B. Bouma, *Handbook of optical coherence tomography* (CRC Press, 2001).
3. W. Drexler and J. G. Fujimoto, *Optical coherence tomography: technology and applications* (Springer Science & Business Media, 2008).
4. W. Drexler, U. Morgner, F. Kärtner, C. Pitris, S. Boppart, X. Li, E. Ippen, and J. Fujimoto, "In vivo ultrahigh-resolution optical coherence tomography," Opt. Lett. **24**, 1221–1223 (1999).
5. A. G. Podoleanu, G. M. Dobre, and D. A. Jackson, "En-face coherence imaging using galvanometer scanner modulation," Opt. Lett. **23**, 147–149 (1998).
6. C. K. Hitzenberger, "Optical coherence tomography in optics express," Opt. Express **26**, 24240–24259 (2018).
7. J. Fujimoto and E. Swanson, "The development, commercialization, and impact of optical coherence tomography," Invest. Ophthalmol. Vis. Sci. **57**, OCT1–OCT13 (2016).
8. C. O'Mahony, M. Hill, M. Brunet, R. Duane, and A. Mathewson, "Characterization of micromechanical structures using white-light interferometry," Meas. Sci. Technol. **14**, 1807–1814 (2003).
9. J. F. De Boer, B. Cense, B. H. Park, M. C. Pierce, G. J. Tearney, and B. E. Bouma, "Improved signal-to-noise ratio in spectral-domain compared with time-domain optical coherence tomography," Opt. Lett. **28**, 2067–2069 (2003).
10. R. Leitgeb, C. K. Hitzenberger, and A. F. Fercher, "Performance of fourier domain vs. time domain optical coherence tomography," Opt. Express **11**, 889–894 (2003).
11. D. P. Popescu, C. Flueraru, Y. Mao, S. Chang, J. Disano, S. Sherif, and M. G. Sowa, "Optical coherence tomography: fundamental principles, instrumental designs and biomedical applications," Biophys. Rev. **3**, 155–169 (2011).
12. B. I. Erkmen and J. H. Shapiro, "Ghost imaging: from quantum to classical to computational," Adv. Opt. Photonics **2**, 405–450 (2010).
13. M. J. Padgett and R. W. Boyd, "An introduction to ghost imaging: quantum and classical," Phil. Trans. R. Soc. A **375**, 20160233 (2017).
14. K. W. C. Chan, M. N. O'Sullivan, and R. W. Boyd, "Two-color ghost imaging," Phys. Rev. A **79**, 033808 (2009).
15. R. S. Bennink, S. J. Bentley, R. W. Boyd, and J. C. Howell, "Quantum and classical coincidence imaging," Phys. Rev. Lett. **92**, 033601 (2004).
16. R. S. Bennink, S. J. Bentley, and R. W. Boyd, ""Two-photon" coincidence imaging with a classical source," Phys. Rev. Lett. **89**, 113601 (2002).
17. F. Ferri, D. Magatti, A. Gatti, M. Bache, E. Brambilla, and L. A. Lugiato, "High-resolution ghost image and ghost diffraction experiments with thermal light," Phys. Rev. Lett. **94**, 183602 (2005).
18. B. Sun, M. P. Edgar, R. Bowman, L. E. Vittert, S. Welsh, A. Bowman, and M. Padgett, "3D computational imaging with single-pixel detectors," Science **340**, 844–847 (2013).
19. D. Shi, C. Fan, P. Zhang, J. Zhang, H. Shen, C. Qiao, and Y. Wang, "Adaptive optical ghost imaging through atmospheric turbulence," Opt. Express **20**, 27992–27998 (2012).
20. P. Ryczkowski, M. Barbier, A. T. Friberg, J. M. Dudley, and G. Genty, "Ghost imaging in the time domain," Nat. Photonics **10**, 167–170 (2016).
21. F. Devaux, P.-A. Moreau, S. Denis, and E. Lantz, "Computational temporal ghost imaging," Optica **3**, 698–701 (2016).
22. H. Wu, P. Ryczkowski, A. T. Friberg, J. M. Dudley, and G. Genty, "Temporal ghost imaging using wavelength conversion and two-color detection," Optica **6**, 902–906 (2019).
23. C. Amiot, P. Ryczkowski, A. T. Friberg, J. M. Dudley, and G. Genty, "Supercontinuum spectral-domain ghost imaging," Opt. Lett. **43**, 5025–5028 (2018).
24. J. M. Dudley, G. Genty, and S. Coen, "Supercontinuum generation in photonic crystal fiber," Rev. Mod. Phys. **78**, 1135–1184 (2006).
25. B. Wetzel, A. Stefani, L. Larger, P.-A. Lacourt, J.-M. Merolla, T. Sylvestre, A. Kudlinski, A. Mussot, G. Genty, and F. Dias, "Real-time full bandwidth measurement of spectral noise in supercontinuum generation," Sci. Rep. **2**, 882 (2012).
26. K. Goda and B. Jalali, "Dispersive Fourier transformation for fast continuous single-shot measurements," Nat. Photonics **7**, 102–112 (2013).

27. A. Mahjoubfar, D. V. Churkin, S. Barland, N. Broderick, S. K. Turitsyn, and B. Jalali, "Time stretch and its applications," Nat. Photonics **11**, 341–351 (2017).
28. T. Godin, B. Wetzel, T. Sylvestre, L. Larger, A. Kudlinski, A. Mussot, A. B. Salem, M. Zghal, G. Genty, and F. Dias, "Real time noise and wavelength correlations in octave-spanning supercontinuum generation," Opt. Express **21**, 18452–18460 (2013).
29. S. M. Kolenderska, O. Katz, M. Fink, and S. Gigan, "Scanning-free imaging through a single fiber by random spatio-spectral encoding," Opt. Lett. **40**, 534–537 (2015).